R-matrix electron-impact excitation data for B-like Si and its application in cool stars

G. Y. Liang, A. D. Whiteford, and N. R. Badnell

Department of Physics, University of Strathclyde, Glasgow, G4 0NG, UK
e-mail: guiyun.liang@strath.ac.uk

ABSTRACT

We present the results of an intermediate coupling frame-transformation R-matrix calculation for the electron-impact excitation of Si^{9+}. The target and close-coupling expansions are both taken to be the 125 fine-structure levels (58 LS terms) belonging to the configurations $2s^x2p^y$ ($x+y = 3$) and $2s^\alpha 2p^\beta 3l$ ($\alpha+\beta = 2$, $l = s$, p, and d). Due to the additional resonances included in our calculation, we find significant differences at low temperatures with the widely used $n = 2 \rightarrow 2$ excitation rates, also obtained with the R-matrix method, as well as with the $n = 2 \rightarrow 3$ excitation rates calculated by using the distorted wave (DW) approximation. We present a list of prominent transition lines and comparisons with SERTS and Hinode/EIS EUV spectra of the solar corona, SUMER observations for the quiet sun, as well as *Chandra* LETG and Rocket soft X-ray spectra of the Procyon corona and solar flares, respectively. Line emissivities of some transitions are enhanced up to 40% when compared with those obtained from using the previous atomic data at the same electron density (1.6×10^9 cm^{-3}) and temperature (1.3×10^6 K). The comparison with *Chandra* LETG observation of Procyon reveals that the 3s−2p line flux was significantly underestimated (by a factor of 4−5) in previous analyses. Some EUV and soft X-ray emission line ratios are n_e-sensitive and T_e-insensitive. Estimated electron densities from them shift downwards due to the new resonant-enhanced excitation data used in the present modelling.

Key words. atomic data – atomic processes – plasmas – stars: coronae – X-rays: stars – ultraviolet: solar system

1. Introduction

Since the launch of the first space station solar science experiment *Skylab*[1], a number of space missions carrying EUV and X-ray spectrometers with a spectral resolution of typically 30−80 mÅ have been launched so far: the Solar EUV Rocket Telescope and Spectrograph (SERTS)[2], the instrument of Solar Ultraviolet Measurements of Emitted Radiation (SUMER) on the Solar & Heliospheric Observatory (SOHO)[3], the Cosmic Hot Interstellar Plasma Spectrometer (CHIPS)[4], *Chandra* X-ray observatory[5], XMM-Newton[6], and the new generation solar observatory *Hinode* (Solar-B)[7]. A large number of emission lines have been reported and identified for astrophysical objects from observations made with these satellites. The next generation X-ray satellite – International X-ray Observatory (IXO, previously named Con-X)[8], has a much higher spectral resolution and its collection area will be enhanced by two orders of magnitude over the present generation. Many more emission lines will be identified, and blended emissions will be resolved with the high-resolution spectrometer on-board the IXO.

Many emission lines show density and temperature diagnostic potential for astrophysical and laboratory plasmas. In particular, intensity ratios of 2p−2s and 3d−2p transition lines in the B-like sequence are excellent electron density (n_e) diagnostics (Flower & Nussbaumer 1975; Phillips et al. 1996) due to their close wavelengths and, hence, low uncertainty in their relative intensity calibration. In fact, many useful line ratios of EUV emission lines from 2p−2s transitions have been reported in the literature. For example: Si X (Keenan et al. 2000), Ar XIV (Keenan et al. 2003) and Fe XXII (Phillips et al. 1996; Wargelin et al. 1998, who also discussed the density sensitivity of the X-ray lines). Liang & Zhao (2008a) reported a density-sensitive line ratio of soft X-ray emission lines arising from 3d−2p transitions for these ions based on the results of distorted wave (DW) calculations for $n = 2 \rightarrow 3$ excitations.

However, some discrepancies between predicted and observed line intensities from a number of ions have been reported. For example, Audard et al. (2001) demonstrated the discrepancies between modelling and the XMM-Newton observation for Capella, in particular emission lines in range of 20−38 Å. In modelling laboratory spectroscopy of highly-charged argon and sulphur with the Hebrew University Lawrence Livermore Atomic Code (HULLAC; Bar-Shalom et al. 1988), Lepson et al. (2003, 2005) demonstrated that there are large discrepancies between the laboratory measurements and the HULLAC simulation. Liang et al. (2008b) reported a line list for highly charged Si ions including Si X, and their comparison with observed values for the Procyon corona showing discrepancies. In particular, the 3s−2p transition lines are underestimated significantly when compared with the 3d−2p transition lines. This type of discrepancy has been reported in laboratory plasmas as well, such as for the case of Ne-like Fe and Ni (Beiersdorfer et al. 2002, 2004; Gu et al. 2004). Large discrepancies also appear

---

[1] http://solarscience.msfc.nasa.gov/Skylab.shtml
[2] http://serts.gsfc.nasa.gov/index.shtml
[3] http://sohowww.nascom.nasa.gov/home.html
[4] http://chips.ssl.berkeley.edu/
[5] http://chandra.harvard.edu/
[6] http://xmm.vilspa.esa.es/
[7] http://solarb.msfc.nasa.gov/
[8] http://ixo.gsfc.nasa.gov/

for the emission spectra from other intermediate-charged ions, such as Fe XVIII and Fe XIX, as reported by Desai et al. (2005) based on the *Chandra* observation of Capella. The inclusion of resonant-excitation processes enhances the 3s−2p line intensity of Fe XVII by 57% at an electron temperature of 600 eV, which greatly reduces the discrepancy between astrophysical observations and theoretical predictions (Doron & Behar 2002). For Fe XVIII, the discrepancy was satisfactorily explained later by Del Zanna (2006) when accurate *R*-matrix excitation data was adopted (Witthoeft et al. 2006). So, a description of electron-impact excitation including such resonances can be expected to be necessary for other L-shell ions for the satisfactory diagnostic modelling of plasmas.

R-matrix calculations for the electron-impact excitation of Si^{9+} were performed by Zhang et al. (1994) including just the $n = 2$ configurations, furthermore, they presented results for only a subset of transitions and over a limited temperature range. They determined *LS*-coupling scattering matrices and then generated level-resolved results both by purely algebraic recoupling and by term-coupling so as to allow for relativistic effects. Griffin et al. (1998) have shown that term coupling the physical scattering matrices can lead to large inaccuracies at low energies, while term coupling the unphysical scattering matrices resultant from the use of multi-channel quantum defect theory (MQDT) leads to results that are equivalent to those from a full Breit-Pauli *R*-matrix calculation, for all diagnostic purposes. However, the data[9] of Zhang et al. (1994) is widely used by the astrophysical community, for example, CHIANTI v.5 (Landi et al. 2006) and APEC (Smith et al. 2001). Later, Keenan et al. (2000) repeated the term-coupling *R*-matrix calculation of Zhang et al. (1994), correcting a slight error in the term-coupling, and presented results for all 105 $n = 2 \rightarrow 2$ inelastic transitions, over a wide range of temperatures. For excitations to higher levels, belonging to $n = 3$ configurations, results of a DW calculation by Zhang & Sampson (1994) were included in the CHIANTI-5.2 database. By using a larger configuration interaction (CI) target, Liang et al. (2007) calculated results for excitations up to $n = 5$ using the flexible atomic code FAC of Gu (2003).

Here, we present results for a complete set of electron-impact excitations involving $n = 2$ and 3 levels, calculated using the *R*-matrix intermediate coupling frame transformation (ICFT) approach, as described in Sect. 2. We then investigate the reported discrepancies between observed and predicted line intensities in the solar and Procyon coronae in Sect. 3. In Sect. 4, we estimate the electron density of some astrophysical plasmas, for example the solar active region and the Procyon corona. We summarize our findings in Sect. 5. Our work is a part of on-going collaborative work – the UK atomic processes for astrophysical plasmas (APAP) Network[10], a broadening of scope of the original UK RmaX Network.

2. Calculation

2.1. Target structure

Our target structure is based on the following configurations: $2s^x 2p^y$ ($x + y = 3$) and $2s^\alpha 2p^\beta 3l$ ($\alpha + \beta = 2$, $l = s$, p and d). The orbital basis functions (1s−3d) were obtained from AUTOSTRUCTURE (Badnell 1997) using the Thomas-Femi-Dirac-Amaldi model potential. The scaling parameters
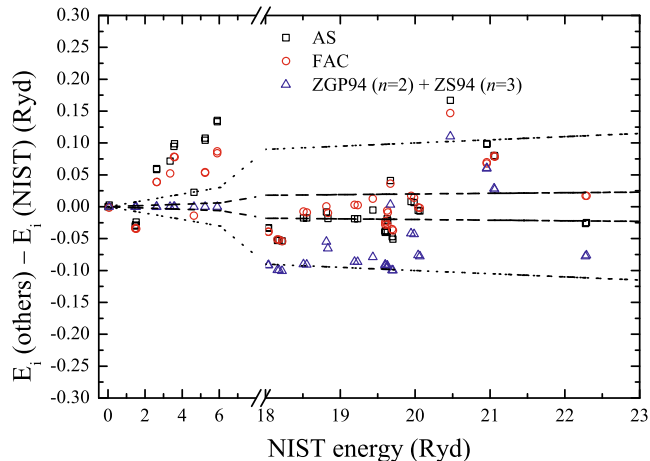

Fig. 1. Theoretical energy levels from the present AUTOSTRUCTURE (AS) and FAC calculations, as well as those of Zhang et al. (1994), Zhang & Sampson (1994) compared with the observed taken from the NIST v.3 database. The dashed and dotted lines correspond to agreement within 0.1% and 0.5%, respectively. (*Colour online.*)

were obtained by minimizing the equally-weighted sum of all 58 LS term energies. We then included the one-body mass-velocity, spin-orbit, and Darwin relativistic corrections. (No valence electron two-body fine-structure operators were included, in line with their absence from the standard *R*-matrix code.) The resultant theoretical target energies (125 fine-structure) are listed in Table 1 along with the level identification and the observed values taken from the NIST v3 database[11], as well as theoretical results of Zhang & Sampson (1994) for $n = 3$ levels and data from Zhang et al. (1994) for $n = 2$ levels (the low-lying ones used are the observed). These theoretical energies were used by the present version (5.2) of CHIANTI[12] (Landi et al. 2006). With a few exceptions in the lower levels and the $2s2p3d\ ^2S_{1/2}$, $2s2p3d\ ^2F_{3/2,5/3}$, $^2D_{3/2}$ levels, excellent agreement (within 0.2%) between the results of the AUTOSTRUCTURE calculation and observed energy levels is obtained, and we illustrate this in Fig. 1. This agreement is an improvement on that of the theoretical results of Zhang & Sampson (1994). The results obtained from FAC also show good agreement with the NIST values.

The full set of radiative transition rates $A_{i,j}(s^{-1})$ amongst the 125 levels was calculated with AUTOSTRUCTURE. Comparisons with the data available in CHIANTI (654 transitions to the 15 lowest-lying levels) show differences of less than 20% and a factor of 2 for 39% and 71% of the total transitions, respectively. For decays from the 59 lowest-lying levels to the ground state, the differences are less than 20% for two-thirds of transitions (cf. Table 2), and agree better with the data compiled by NIST v.3 (from Cavalcanti et al. 2000).

2.2. Collision strengths

For the electron-impact excitation calculation, we employ the *R*-matrix intermediate-coupling frame transformation method of Griffin et al. (1998). The calculation follows similar procedures for the Iron Project work on Ca-like Fe by Witthoeft & Badnell (2008).

Table 1. Energy levels (in Ryd) of Si^{9+}.

ID	Conf.	$^{2S+1}L_J^\pi$	NIST[a]	AS[b]	FAC[c]	ZS94[d]	ID	Conf.	$^{2S+1}L_J^\pi$	NIST[a]	AS	FAC	ZS94
1	$2s^2 2p$	$^2P^o_{1/2}$					64	$2p^2 3s$	$^4P^e_{3/2}$		20.8084	20.8434	20.7610
2	$2s^2 2p$	$^2P^o_{3/2}$	0.0637	0.0664	0.0623	0.0637	65	$2p^2 3s$	$^4P^e_{5/2}$		20.8453	20.8776	20.7951
3	$2s2p^2$	$^4P^e_{1/2}$	1.4672	1.4370	1.4335	1.4672	66	$2s2p3d$	$^2F^o_{7/2}$	20.9582	21.0562	21.0263	21.0180
4	$2s2p^2$	$^4P^e_{3/2}$	1.4898	1.4610	1.4567	1.4898	67	$2s2p3d$	$^2F^o_{5/2}$	20.9582	21.0575	21.0282	21.0191
5	$2s2p^2$	$^4P^e_{5/2}$	1.5224	1.4985	1.4880	1.5224	68	$2s2p3d$	$^2D^o_{3/2}$	21.0551	21.1356	21.1353	21.0838
6	$2s2p^2$	$^2D^e_{3/2}$	2.6231	2.6815	2.6620	2.6231	69	$2s2p3d$	$^2D^o_{5/2}$	21.0629	21.1425	21.1416	21.0900
7	$2s2p^2$	$^2D^e_{5/2}$	2.6234	2.6833	2.6622	2.6234	70	$2p^2 3s$	$^2P^e_{1/2}$		21.2186	21.2463	21.1318
8	$2s2p^2$	$^2S^e_{1/2}$	3.3505	3.4221	3.4029	3.3505	71	$2p^2 3s$	$^2P^e_{3/2}$		21.2590	21.2825	21.1699
9	$2s2p^2$	$^2P^e_{1/2}$	3.5543	3.6491	3.6325	3.5543	72	$2s2p3d$	$^2P^o_{1/2}$		21.2731	21.2686	21.2200
10	$2s2p^2$	$^2P^e_{3/2}$	3.5907	3.6895	3.6687	3.5907	73	$2s2p3d$	$^2P^o_{3/2}$		21.2800	21.2732	21.2246
11	$2p^3$	$^4S^o_{3/2}$	4.6414	4.6641	4.6274	4.6414	74	$2p^2 3p$	$^2S^o_{1/2}$		21.2878	21.3255	21.2422
12	$2p^3$	$^2D^o_{3/2}$	5.2437	5.3479	5.2973	5.2437	75	$2p^2 3p$	$^4D^o_{1/2}$		21.3792	21.4234	21.3370
13	$2p^3$	$^2D^o_{5/2}$	5.2439	5.3517	5.2984	5.2439	76	$2p^2 3p$	$^4D^o_{3/2}$		21.3931	21.4355	21.3510
14	$2p^3$	$^2P^o_{1/2}$	5.8937	6.0271	5.9806	5.8937	77	$2p^2 3p$	$^4D^o_{5/2}$		21.4168	21.4567	21.3744
15	$2p^3$	$^2P^o_{3/2}$	5.8994	6.0348	5.9832	5.8995	78	$2p^2 3s$	$^2D^e_{5/2}$		21.4443	21.4737	21.3951
16	$2s^2 3s$	$^2S^e_{1/2}$		16.5450	16.5368	16.4970	79	$2p^2 3s$	$^2D^e_{3/2}$		21.4455	21.4748	21.3956
17	$2s^2 3p$	$^2P^o_{1/2}$		17.2856	17.2881	17.2366	80	$2p^2 3p$	$^4D^o_{7/2}$		21.4503	21.4879	21.4061
18	$2s^2 3p$	$^2P^o_{3/2}$		17.3019	17.3046	17.2548	81	$2p^2 3p$	$^4P^o_{1/2}$		21.4860	21.5255	21.4449
19	$2s^2 3d$	$^2D^e_{3/2}$	18.0363	18.0030	17.9972	17.9443	82	$2p^2 3p$	$^4P^o_{3/2}$		21.4956	21.5349	21.4531
20	$2s^2 3d$	$^2D^e_{5/2}$	18.0406	18.0078	18.0014	17.9493	83	$2p^2 3p$	$^4P^o_{5/2}$		21.5166	21.5535	21.4733
21	$2s2p3s$	$^4P^o_{1/2}$	18.1600	18.1070	18.1088	18.0608	84	$2p^2 3p$	$^2D^o_{3/2}$		21.5945	21.6406	21.5462
22	$2s2p3s$	$^4P^o_{3/2}$	18.1810	18.1289	18.1293	18.0818	85	$2p^2 3p$	$^2D^o_{5/2}$		21.6397	21.6836	21.5903
23	$2s2p3s$	$^4P^o_{5/2}$	18.2215	18.1681	18.1675	18.1209	86	$2p^2 3p$	$^4S^o_{3/2}$		21.7785	21.8273	21.6973
24	$2s2p3s$	$^2P^o_{1/2}$	18.5084	18.4910	18.5012	18.4184	87	$2p^2 3p$	$^2P^o_{3/2}$		21.7866	21.8347	21.7384
25	$2s2p3s$	$^2P^o_{3/2}$	18.5521	18.5346	18.5431	18.4615	88	$2p^2 3p$	$^2P^o_{1/2}$		21.7908	21.8588	21.7342
26	$2s2p3p$	$^4D^e_{1/2}$		18.7682	18.7772	18.7209	89	$2p^2 3d$	$^4F^e_{3/2}$		21.9403	21.9761	21.8967
27	$2s2p3p$	$^4D^e_{3/2}$		18.7885	18.7954	18.7405	90	$2p^2 3d$	$^4F^e_{5/2}$		21.9537	21.9902	21.9094
28	$2s2p3p$	$^2P^e_{1/2}$	18.8139	18.8058	18.8146	18.7593	91	$2p^2 3d$	$^4F^e_{7/2}$		21.9731	22.0079	21.9278
29	$2s2p3p$	$^2P^e_{3/2}$	18.8336	18.8152	18.8238	18.7683	92	$2p^2 3d$	$^4F^e_{9/2}$		21.9993	22.0288	21.9520
30	$2s2p3p$	$^4D^e_{5/2}$		18.8220	18.8269	18.7769	93	$2p^2 3p$	$^2F^o_{5/2}$		22.0439	22.0825	22.0050
31	$2s2p3p$	$^4D^e_{7/2}$		18.8560	18.8607	18.8121	94	$2p^2 3p$	$^2F^o_{7/2}$		22.0554	22.0939	22.0171
32	$2s2p3p$	$^4S^e_{3/2}$		18.9487	18.9586	18.9056	95	$2p^2 3d$	$^2P^e_{3/2}$		22.0733	22.1139	22.0267
33	$2s2p3p$	$^4P^e_{1/2}$		19.0525	19.0822	18.9858	96	$2p^2 3d$	$^4D^e_{1/2}$		22.0776	22.1154	22.0355
34	$2s2p3p$	$^4P^e_{3/2}$		19.0711	19.0993	19.0046	97	$2p^2 3d$	$^4D^e_{5/2}$		22.0953	22.1334	22.0516
35	$2s2p3p$	$^4P^e_{5/2}$		19.0913	19.1179	19.0227	98	$2p^2 3d$	$^4D^e_{3/2}$		22.1032	22.1447	22.0571
36	$2s2p3p$	$^2D^e_{3/2}$	19.1890	19.1704	19.1919	19.1028	99	$2p^2 3d$	$^4D^e_{7/2}$		22.1066	22.1403	22.0621
37	$2s2p3p$	$^2D^e_{5/2}$	19.2301	19.2114	19.2327	19.1437	100	$2p^2 3d$	$^2P^e_{1/2}$		22.1345	22.1755	22.0831
38	$2s2p3d$	$^4F^o_{3/2}$		19.3897	19.3973	19.3414	101	$2p^2 3d$	$^2F^e_{5/2}$		22.1703	22.2021	22.1259
39	$2s2p3d$	$^4F^o_{5/2}$		19.4030	19.4121	19.3544	102	$2p^2 3d$	$^2F^e_{7/2}$		22.2179	22.2450	22.1725
40	$2s2p3d$	$^4F^o_{7/2}$		19.4226	19.4318	19.3738	103	$2p^2 3d$	$^4P^e_{5/2}$	22.2756	22.2494	22.2927	22.1978
41	$2s2p3d$	$^2S^e_{1/2}$	19.4337	19.4284	19.4463	19.3548	104	$2p^2 3p$	$^2D^o_{5/2}$		22.2642	22.3481	22.1825
42	$2s2p3d$	$^4F^o_{9/2}$		19.4499	19.4548	19.4014	105	$2p^2 3d$	$^4P^e_{3/2}$	22.2896	22.2649	22.3069	22.2135
43	$2s2p3d$	$^4D^o_{1/2}$	19.6004	19.5602	19.5722	19.5081	106	$2p^2 3p$	$^2D^o_{3/2}$		22.2651	22.3514	22.1856
44	$2s2p3d$	$^4D^o_{3/2}$	19.6004	19.5622	19.5757	19.5096	107	$2p^2 3d$	$^4P^e_{1/2}$		22.2731	22.3158	22.2216
45	$2s2p3d$	$^4D^o_{5/2}$	19.6046	19.5664	19.5820	19.5130	108	$2p^2 3s$	$^2S^e_{1/2}$		22.4339	22.4660	22.4001
46	$2s2p3d$	$^4D^o_{7/2}$	19.6271	19.5879	19.5997	19.5349	109	$2p^2 3p$	$^2P^o_{1/2}$		22.4519	22.5090	22.3612
47	$2s2p3d$	$^2D^o_{3/2}$	19.6260	19.6072	19.6198	19.5313	110	$2p^2 3p$	$^2P^o_{3/2}$		22.4792	22.5387	22.3865
48	$2s2p3d$	$^2D^o_{5/2}$	19.6331	19.6112	19.6240	19.5390	111	$2p^2 3d$	$^2D^e_{3/2}$		22.5927	22.6130	22.5328
49	$2s2p3d$	$^4P^o_{5/2}$	19.6917	19.6450	19.6568	19.5923	112	$2p^2 3d$	$^2D^e_{5/2}$		22.5934	22.6147	22.5347
50	$2s2p3d$	$^4P^o_{3/2}$	19.7025	19.6516	19.6655	19.6026	113	$2p^2 3d$	$^2G^e_{7/2}$		22.6011	22.6272	22.5608
51	$2s2p3d$	$^4P^o_{1/2}$		19.6576	19.6736	19.6098	114	$2p^2 3d$	$^2G^e_{9/2}$		22.6062	22.6303	22.5653
52	$2s2p3s$	$^2P^o_{1/2}$		19.7078	19.7031	19.6708	115	$2p^2 3d$	$^2D^e_{3/2}$		22.7474	22.7877	22.7047
53	$2s2p3s$	$^2P^o_{3/2}$	19.6682	19.7092	19.7045	19.6714	116	$2p^2 3d$	$^2D^e_{5/2}$		22.7651	22.8000	22.7200
54	$2s2p3d$	$^2F^o_{5/2}$	19.9439	19.9522	19.9611	19.9023	117	$2p^2 3d$	$^2F^e_{7/2}$		22.8084	22.8288	22.7608
55	$2s2p3d$	$^2F^o_{7/2}$	19.9858	19.9925	19.9999	19.9430	118	$2p^2 3d$	$^2F^e_{5/2}$		22.8222	22.8440	22.7754
56	$2s2p3d$	$^2P^o_{3/2}$	20.0407	20.0350	20.0399	19.9648	119	$2p^2 3d$	$^2P^e_{1/2}$		22.9527	22.9918	22.8744
57	$2s2p3d$	$^2P^o_{1/2}$	20.0642	20.0575	20.0621	19.9866	120	$2p^2 3d$	$^2P^e_{3/2}$		22.9693	23.0067	22.8888
58	$2s2p3p$	$^2P^e_{1/2}$		20.4168	20.4263	20.3749	121	$2p^2 3d$	$^2S^e_{1/2}$		23.0395	23.0746	23.0057
59	$2s2p3p$	$^2P^e_{3/2}$		20.4271	20.4346	20.3836	122	$2p^2 3p$	$^2P^o_{1/2}$		23.1746	23.2319	23.1418

Table 1. continued.

ID	Conf.	$^{2S+1}L_J^\pi$	NIST[a]	AS[b]	FAC[c]	ZS94[d]	ID	Conf.	$^{2S+1}L_J^\pi$	NIST[a]	AS	FAC	ZS94
60	2s2p3p	$^2D_{3/2}^e$		20.4412	20.4468	20.3963	123	2p^{2}3p	$^2P_{3/2}^o$		23.1805	23.2360	23.1486
61	2s2p3p	$^2D_{5/2}^e$		20.4424	20.4463	20.3977	124	2p^{2}3d	$^2D_{5/2}^e$		23.7640	23.7756	23.7376
62	2s2p3p	$^2S_{1/2}^e$	20.4698	20.6368	20.6169	20.5801	125	2p^{2}3d	$^2D_{3/2}^e$		23.7716	23.7839	23.7456
63	2p^{2}3s	$^4P_{1/2}^e$		20.7850	20.8237	20.7382							

[a] http://physics.nist.gov/PhysRefData/ASD/levels_form.html; [b] AUTOSTRUCTURE (present work); [c] Liang et al. (2007); [d] Zhang &
Sampson (1994), their 15 lowest-lying levels are observed values from Zhang et al. (1994).

Table 2. Radiative decay rates ($A_{i,j}$ for $i \leftarrow j$ transition in units of s^{-1})
for transitions to the ground level.

low	upper	AS[a]	ZS94[b]	NIST[c]
1	3	3.267(05)[d]	3.020(05)	2.99(05)
1	6	1.964(09)	1.850(09)	1.91(09)
1	8	5.185(09)	4.940(09)	5.07(09)
1	9	9.271(09)	8.850(09)	9.23(09)
1	10	2.781(09)	2.740(09)	2.78(09)
1	16	5.509(10)	4.386(10)	
1	19	8.032(11)	7.378(11)	8.15(11)
1	26	1.262(11)	1.063(11)	
1	27	3.009(10)	2.922(10)	
1	28	1.586(11)	1.163(11)	2.66(11)
1	29	5.266(10)	3.723(10)	7.27(10)
1	32	1.582(09)	1.293(09)	
1	33	5.395(08)	6.594(08)	
1	34	3.205(08)	2.747(08)	
1	36	3.433(11)	3.217(11)	3.61(11)
1	41	1.290(11)	1.400(11)	1.29(11)
1	58	6.518(10)	9.096(10)	
1	59	2.365(09)	1.386(09)	
1	60	4.053(10)	4.827(10)	
1	62	2.720(10)	1.353(10)	2.15(10)
1	63	3.811(08)	2.987(08)	
1	64	4.958(06)	6.865(06)	
1	70	2.789(10)	3.705(10)	
1	71	8.517(09)	1.103(10)	
1	79	4.453(09)	6.434(09)	
1	95	9.367(08)	1.969(09)	
1	96	6.778(08)	1.574(09)	
1	98	6.217(08)	7.689(08)	
1	100	4.124(09)	7.050(09)	
1	108	2.976(09)	3.747(09)	
1	111	1.482(10)	3.010(10)	
1	115	8.574(09)	1.538(10)	
1	119	9.798(09)	1.579(10)	
1	120	2.011(09)	3.116(09)	
1	121	1.649(09)	5.421(09)	
1	125	1.955(09)	4.028(09)	

[a] AUTOSTRUCTURE (present work); [b] Zhang & Sampson (1994);
[c] NIST v3 (from Cavalcanti et al. 2000); [d] (m) denotes $\times 10^m$.

We used 40 continuum basis per orbital angular momentum.
Contributions from partial waves up to $J = 12$ were included
in the exchange calculation. The contributions from higher par-
tial waves up to $J = 42$ were included via a non-exchange cal-
culation. A "top-up" was used to complete the partial collision
strength sum over higher J-values by using the Burgess sum rule
(Burgess 1974) for dipole transitions and a geometric series for
the non-dipole transitions (Badnell & Griffin 2001). In the outer-
region exchange calculation, we used an energy mesh step of
$2 \times 10^{-6} z^2$ Ryd through the resonance region (from threshold to

24 Ryd), where z is the residual charge of the ion (9 in present
case). Beyond the resonance region (from 24 to 92 Ryd) an en-
ergy step of $2 \times 10^{-4} z^2$ Ryd was used. For the non-exchange
calculation, we used a step of $1 \times 10^{-3} z^2$ Ryd over the entire
energy range. The calculation was carried-out up to an incident
energy of 92 Ryd. Collision strengths $\Omega_{i,j}$ were obtained for all
7750 inelastic transitions between the 125 levels.

Observed and semi-empirically adjusted energies were used
for the 69 lowest-lying levels. For those 26 observed levels miss-
ing from the NIST database, we first derived the mean value
of differences between our level energies and the correspond-
ing NIST values for available levels of the same configuration,
then we adjusted our calculated level energies by this mean
value. The level energies of the 2s^{2}3s and 2s^{2}3p configurations
were adjusted by the same correction value determined for the
2s^{2}3d configuration, whereas the energy of levels 64 and 65 (be-
longing to the 2p^{2}3s configuration) were adjusted by the same
correction value determined for the 2s2p3d configuration. These
observed and adjusted energies are employed in the MQDT for-
mula which converts from the slowly-varying-with-energy un-
physical **K**-matrix to the strongly (resonant) energy-dependent
physical **K**-matrix. This ensures that Rydberg series of reso-
nances converge on the observed thresholds. In addition, low-
lying (non-correlation) resonances can be expected to be po-
sitioned accurately just above excitation thresholds. A similar
procedure has been demonstrated to be very accurate in the study
of dielectronic recombination, where there is much precise ex-
perimental cross section data with which to compare (see Savin
et al. 2002, for example).

We extend the collision strengths beyond 92 Ryd to the in-
finite energy limits by using the method described by Burgess
& Tully (1992). Born limits (non-dipole allowed) and line-
strengths (dipole) from AUTOSTRUCTURE were used for inter-
polation when Maxwellian-averaging. For the few remaining
forbidden transitions, the collision strength was extrapolated as-
suming a high-energy behaviour $\sim 1/E^2$.

The three 3d−2p transition lines are the strong emission lines
in solar and stellar coronae, and show a good density sensitivity.
So, we illustrate their collision strengths in Figs. 2a−c, along
with the two 3s−2p transitions in Figs. 2e and f, as well as the
transition (2s^{2}2p $^2P_{3/2}$−2s^{2}2p $^2P_{1/2}$, Fig. 2d) which connects the
two sets. Excellent agreement is found between our background
collision strengths and the DW results of Liang et al. (2007).

2.3. Effective collision strengths

Maxwell-averaged effective collision strengths Υ were calcu-
lated over a wide temperature range (1.0×10^4−1.0×10^7 K) to
cover all relevant astrophysical environments. For example, in
collision dominated plasmas, such as stellar coronae, supernova
remnants etc., Si^{9+} has a peak abundance in equilibrium at $1.3 \times$
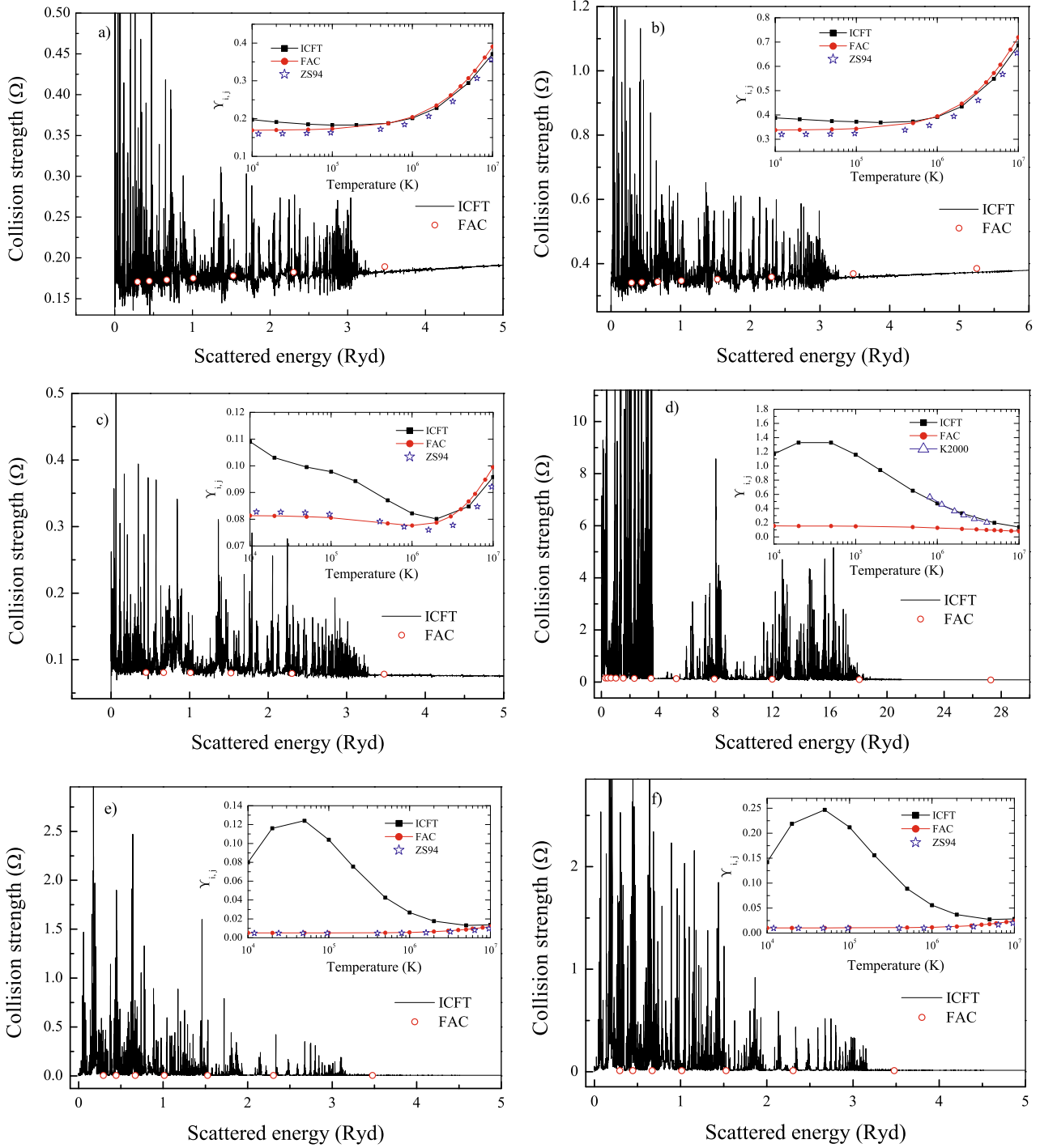10^6 K (Mazzotta et al. 1998; Bryans et al. 2006) using ionization

Fig. 2. Collision strengths calculated using the ICFT *R*-matrix method, along with other available predictions for several important transitions of Si^{9+}. The circle symbols denote the FAC distorted wave (DW) results of Liang et al. (2007). The inset panels illustrate the Maxwellian-averaged effective collision strength (Υ) from the present ICFT *R*-matrix (filled boxes linked by solid lines) and Liang et al.'s (2007) FAC DW (filled circles linked by solid lines) calculations, and data we derived from the original Ω's of Zhang & Sampson (1994, denoted ZS94, opened star symbols). **a)** $2s^22p\ ^2P_{1/2}-2s^23d\ ^2D_{3/2}$ (1–19); **b)** $2s^22p\ ^2P_{3/2}-2s^23d\ ^2D_{5/2}$ (2–20); **c)** $2s^22p\ ^2P_{3/2}-2s^23d\ ^2D_{3/2}$ (2–19); **d)** $2s^22p\ ^2P_{1/2}-2s^22p\ ^2P_{3/2}$ (1–2), the *R*-matrix results of Keenan et al. (2000, denoted K2000, triangle symbols linked by solid lines) are also depicted; **e)** $2s^22p\ ^2P_{1/2}-2s^23s\ ^2S_{1/2}$ (1–16); and **f)** $2s^22p\ ^2P_{3/2}-2s^23s\ ^2S_{1/2}$ (2–16). (*Colour online*.)

and recombination rates applicable to the low-density regime. High electron densities (say ~10^{10} cm^{-3} as found in a solar active region) can shift the peak ion abundance by 20–30%, for example, the ionization equilibrium of Fe^{7+} and Fe^{8+} (see Fig. 10 in Del Zanna & Mason 2003). In typical photoionized plasmas,

the ion formation temperature is much lower, a few times 10^4 K (Kallman & Bautista 2001).

The inset panels in Fig. 2 show Υ. For the 1–19 and 2–20 transitions (see Figs. 2a and b), the *R*-matrix results show good agreement (within 5%) with Liang et al.'s (2007)
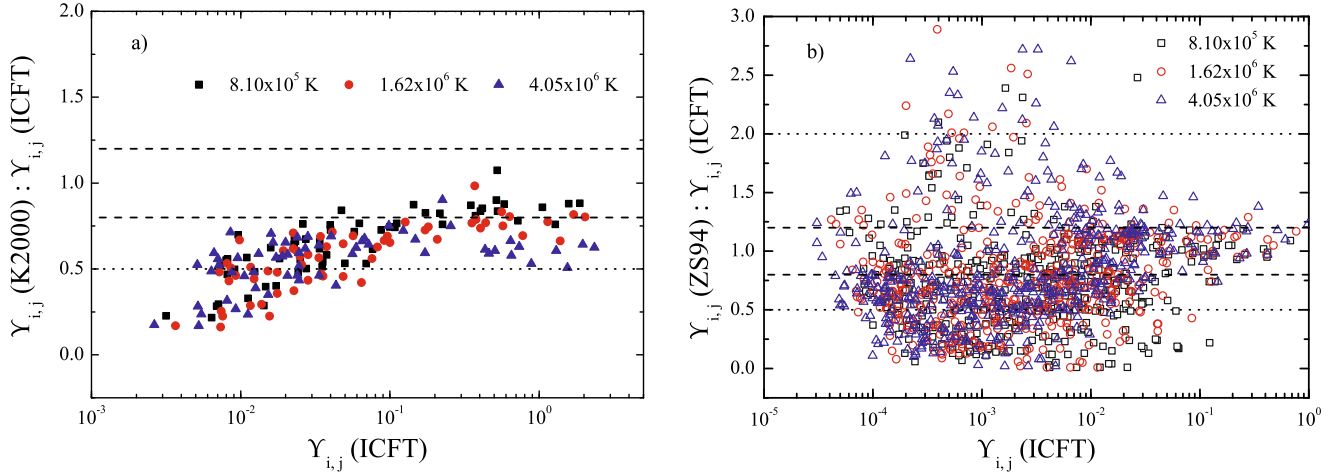
Fig. 3. Comparison of the present ICFT *R*-matrix effective collision strengths with those of previous calculations. **a)** With Keenan et al. (2000), for their $n = 2$ *R*-matrix calculation, to all 14 excited levels of the $n = 2$ configurations, from the lowest 5-lying levels. **b)** With Zhang & Sampson (1994), for their DW calculation, to the $n = 3$ excited levels, from the lowest 5-lying levels. The dashed and dotted lines correspond to agreement within 20% and a factor of 2, respectively (only the lower dotted line is present in **a)**). (*Colour online.*)

DW results obtained using FAC and those that we obtained using the original Ω of Zhang & Sampson (1994) over the entire temperature range. For the 2−19 transition (see Fig. 2c), the present *R*-matrix results are higher than other two DW results, below $T_e = 1.0 \times 10^6$ K, and the difference increases to $\approx 40\%$ at 1.0×10^4 K. But, above $T_e > 10^6$ K, the three predictions demonstrate excellent agreement. This indicates that the resonance effects are weak on Υ for 3d−2p transitions at the temperature of peak Si^{9+} abundance in collisional equilibrium. For the $2s^2 2p\ ^2P_{1/2}-2s^2 2p\ ^2P_{3/2}$ transition, which connects the two sets of 3d−2p transitions (see Figs. 2a and b), the effect of resonances crosses the abundant ion formation temperatures, and on up to 1.0×10^7 K. There is a peak value to our *R*-matrix Υ around $T_e = 4.0 \times 10^4$ K, showing the largest underestimate by the DW calculation. The present *R*-matrix results for the fine structure transition exhibit good agreement (Fig. 2d) with the previous term-coupling *R*-matrix results of Keenan et al. (2000). Turning to the two 3s−2p transitions (Figs. 2e,f), the resonant enhancement of Υ is up to an order of magnitude at the temperature (1.3×10^6 K) of peak ion abundance in collisional equilibrium. This suggests that the large discrepancy reported in stellar coronae may be due to the uncertainty of their adopted atomic data. The difference between the present *R*-matrix results and the DW ones peaks at around 4.0×10^4 K, which is typical of the temperature of abundance in photoionized plasmas.

By way of a scatter plot, we compare the results of the present *R*-matrix calculation with those of the $n = 2-2$ *R*-matrix results of Keenan et al. (2000) in Fig. 3a and the $n = 2-3$ DW results of Zhang & Sampson (1994) Fig. 3b. We illustrate the differences at three temperatures: 8.10×10^5, 1.62×10^6 and 4.05×10^6 K, as shown in Fig. 3. From Fig. 3a, we can see that the results of the previous *R*-matrix calculation are systematically lower than present ones, by $\sim 20\%$. Indeed, the weaker the excitation, the greater the difference, more than a factor of 2 for a group of the weakest excitations. We also note that there is a group of strong excitations ($\Upsilon > 0.1$) with larger differences at high temperature (up-triangle symbols) than that at low temperature. We selected one point (1−6 excitation) from Fig. 3a to explain the reason of the inverse behaviour at high temperature. In Fig. 4, Keenan et al.'s (scaled) results do not appear to be tending to the correct infinite temperature limit, given by $4S/3$ where S is the

line strength. Keenan et al. (2000) do not report radiative data, but there is little reported uncertainty in the literature for this transition. We note that the original data of Zhang et al. (1994) smoothly converges to the limit point, as do the present *R*-matrix results. Moreover the difference between them decreases with increasing temperature. Other randomly selected dipole transitions in this group (Fig. 3a) exhibit the same behaviour.

For excitation to levels of the $n = 3$ configurations, only DW calculations (Zhang & Sampson 1994; Liang et al. 2007) are reported in the literature, to the best of our knowledge. The comparison with Zhang & Sampson's results indicate that there are 66% and 28% of the total ($n = 3$) transitions with the persent Υ being over 20% and a factor of 2 larger, respectively, at a temperature of 8.10×10^5 K (see Fig. 3b). This again demonstrates that resonant enhancement is common and important for excitations to higher levels. For some transitions, agreement within 20% suggests that the resonance effects are weak for these effective collisions strengths, as shown by Figs. 2a−c.

3. Line intensities

By adopting the present $A_{i,j}$ values and ICFT *R*-matrix Υ, we have calculated the line emissivity, ϵ, of Si X at an electron density of 1.6×10^9 cm^{-3} and electron temperature ranging $10^{6.0-6.2}$ K. The density and temperature are typical values for stellar coronae. In the calculation, excitations by collisions with protons are also included by using data of Foster et al. (1997). The method is basically the CHIANTI code, which was modified to use the original Υ instead of their scaled fitted Υ.

The synthetic spectrum of Si X was constructed via convolution with a Gaussian profile with FWHM of 60 mÅ, which is equivalent to an observed line width in the Low Energy Transmission Grating (LETG) *Chandra*[13] observation for Procyon, and the Solar Extreme Ultraviolet Research Telescope Spectrograph (SERTS) observation for the solar corona (see Fig. 5). The synthetic spectrum covers the soft X-ray and EUV regions dominated by $n = 3 \rightarrow 2$ and $n = 2 \rightarrow 2$ transition lines. The reduction of the *Chandra* LETG raw data of
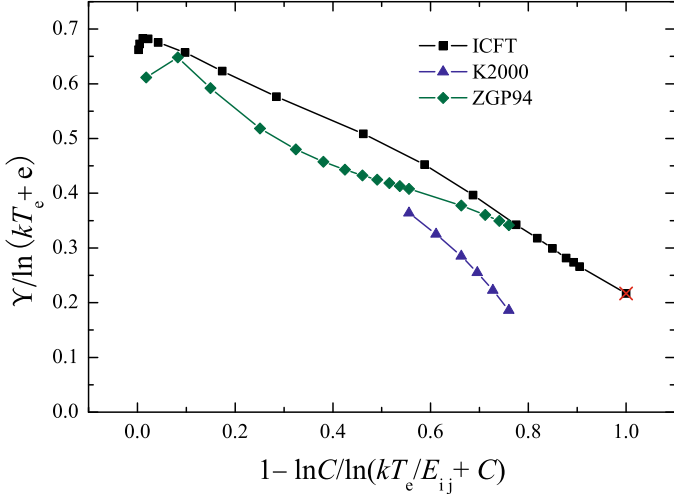
---

[13] http://chandra.harvard.edu/

Fig. 4. Comparison of *R*-matrix scaled effective collision strengths due to Zhang et al. (1994, denoted ZGP94) and Keenan et al. (2000, denoted K2000) with the present ICFT ones for the dipole transition $2s^22p\ ^2P^o_{1/2}-2s2p^2\ ^2D^e_{3/2}$. The scaling accords to the method of Burgess & Tully (1992), using a scaling parameter of $C = 1.8$. (*Colour online*.)

Procyon adopts the CIAO-3.3 software, and follows the procedure described in the work of Liang & Zhao (2008b) to extract the 1D spectrum. For completeness, the soft X-ray observation of solar flare reported by Acton et al. (1985) is also presented in the following analysis (see the 3rd column in Table 3). However, for the SERTS observation, we use the 1D spectrum provided by their website[14] in which subtraction of the background and an absolute calibration have been performed. Thomas & Neupert (1994) reported an increase of line intensities in the SERTS-89 observation for an active region on using a new absolute calibration, which was incorporated into the work of Keenan et al. (2000). The observed line fluxes in these works were used in the present work (see the 2nd column in Table 4). Brown et al. (2008) report the EUV spectroscopy of solar active regions and flares observed with the EUV imaging spectrometer (EIS) onboard the Hinode mission. The corresponding line fluxes are also given in analysis (see the 3rd column in Table 4). In order to illustrate the effect of the new $n = 2 \rightarrow 3$ excitation data, we also calculated the synthetic spectrum using the previous data of Keenan et al. (2000) and Zhang & Sampson (1994).

For the Procyon soft X-ray observation, we further derived the line intensity, I ($=\frac{\epsilon}{4\pi d^2}$EM, where d is the distance to the star, EM is the emission measure, see the 6th and 9th columns in Table 3a) by using the 3-T_e component EM distribution reported by Raassen et al. (2002). For the SERTS observation of an active region, we derived line intensities based upon the observed line flux at 258.37 Å. An illustrative comparison of the relative line intensities between the two different models is presented in Tables 3b, and 4b.

Furthermore, several emission lines of Si X falling at wavelength range of 600−650 Å have been observed by SUMER spectrometer on *SOHO* (Curdt et al. 2004). Their line fluxes are presented in Table 5.

3.1. Chandra LETG observation

For most soft X-ray emission lines, the results of the two calculations show agreement to within 25%, including the strong

---

[14] http://serts.gsfc.nasa.gov/

3d−2p transition lines at 50.524 and 50.691 Å (see the 4th and 7th columns in Table 3a). However, the two weak 3s−2p transition lines, at 54.955 and 55.167 Å are enhanced by a factor of 4−5 when compared with the values calculated using the previous excitation data of Keenan et al. (2000) and Zhang & Sampson (1994). This is due to the strong resonances in the electron-impact excitation, as shown in Figs. 2e and f. In stellar coronal observations there is a large discrepancy of their line intensities, relative to that of the 3d−2p transitions, between the observations and theoretical predictions for Fe XVII−XIX (Desai et al. 2005). Some authors (Schrijver et al. 1994; Schmelz et al. 1997; Saba et al. 1999; Mewe et al. 2001) explain this as being due to stronger opacities in observations of stellar coronae for these strong 3d−2p transitions than for transitions with small gf-values. Here (see Fig. 5, upper pair), we also incorporate a non-solar observation (the LETG spectrum of Procyon – a star of type F5 IV−V, with mass of 1.75 $M_\odot$ and radius of 2.1 $R_\odot$ at a distance of 3.5 pc). The line intensity was normalized according to the intensity of the line at 50.524 Å, see Table 3.

In the Procyon spectrum, an emission line at 55.078 Å was detected (Raassen et al. 2002) with intensity of 0.49 ± 0.06 relative to the 3d−2p line at 50.525 Å, which was assigned to Si IX by Liang & Zhao (2008b). But their predicted flux is still lower than the observation's, by 27%. The present prediction of 0.21 relative to the 3d−2p transition at 50.524 Å satisfactorily explains the discrepancy at 55.078 Å, to within a 1σ statistical error. When compared with the prediction made using the previous excitation data, the line intensity at 55.078 Å is enhanced by a factor of 5. In the solar flare spectra, this emission line was also identified to be Si X (see work of Acton et al. 1985). According to the present prediction, a neighbouring weak emission line at 54.895 Å (see Fig. 5) in Procyon is tentatively assigned to the 3s−2p transition of Si X ($\approx$26% contribution) with a wavelength of 54.955 Å, plus an unknown contribution. In solar flares, its line flux is less than 10 photon cm^{-2} s^{-1} arcsec^{-2}, and unidentified.

We also note that there are two partially blended dipole transition lines ($2s^23p\ ^2P_{3/2,1/2}-2s2p^2\ ^2D_{3/2,5/2}$) at 62.282 Å and 62.358 Å in predicted using the data of Keenan et al. (2000) ($n = 2$) plus Zhang & Sampson (1994) ($n = 3$) which are shifted to 61.925 Å and 61.992 Å (theoretical wavelength), showing better agreement in wavelength with an emission at 61.937 Å in the Procyon observation. This indicates that present structure calculation is more accurate than Zhang & Sampson's work. Moreover, their intensities are enhanced by 44% and 29%, respectively. Liang & Zhao (2008b) identify this emission in Procyon partially from a contribution ($\approx$16%) of a Si VIII line (at 61.792 Å). We predict a co-add line intensity of 0.67 relative to that at 50.525 Å, which satisfactorily explains the discrepancy in the work of Liang & Zhao (2008b). In solar flare spectra, this emission is identified to be Si VIII blending with Mg IX.

At 52.453 and 52.594, as well as 57.309 Å, the results of the two calculations show good agreement with the LETG observation of Procyon, to within 1σ uncertainty. However, in solar flare spectra, 52.453 and 57.309 Å emissions have not been identified, while the 52.594 Å emission was assigned to Ni XVIII. On the short wavelength side in the bottom panel of Fig. 5, the present prediction shows a contribution of 57% to the observed line flux at 47.42 Å. The large discrepancy at the strong n_e-sensitive 3d−2p transition (50.691 Å) is due to a higher value (1.6×10^9 cm^{-3}) adopted, which is from Keenan et al.'s work
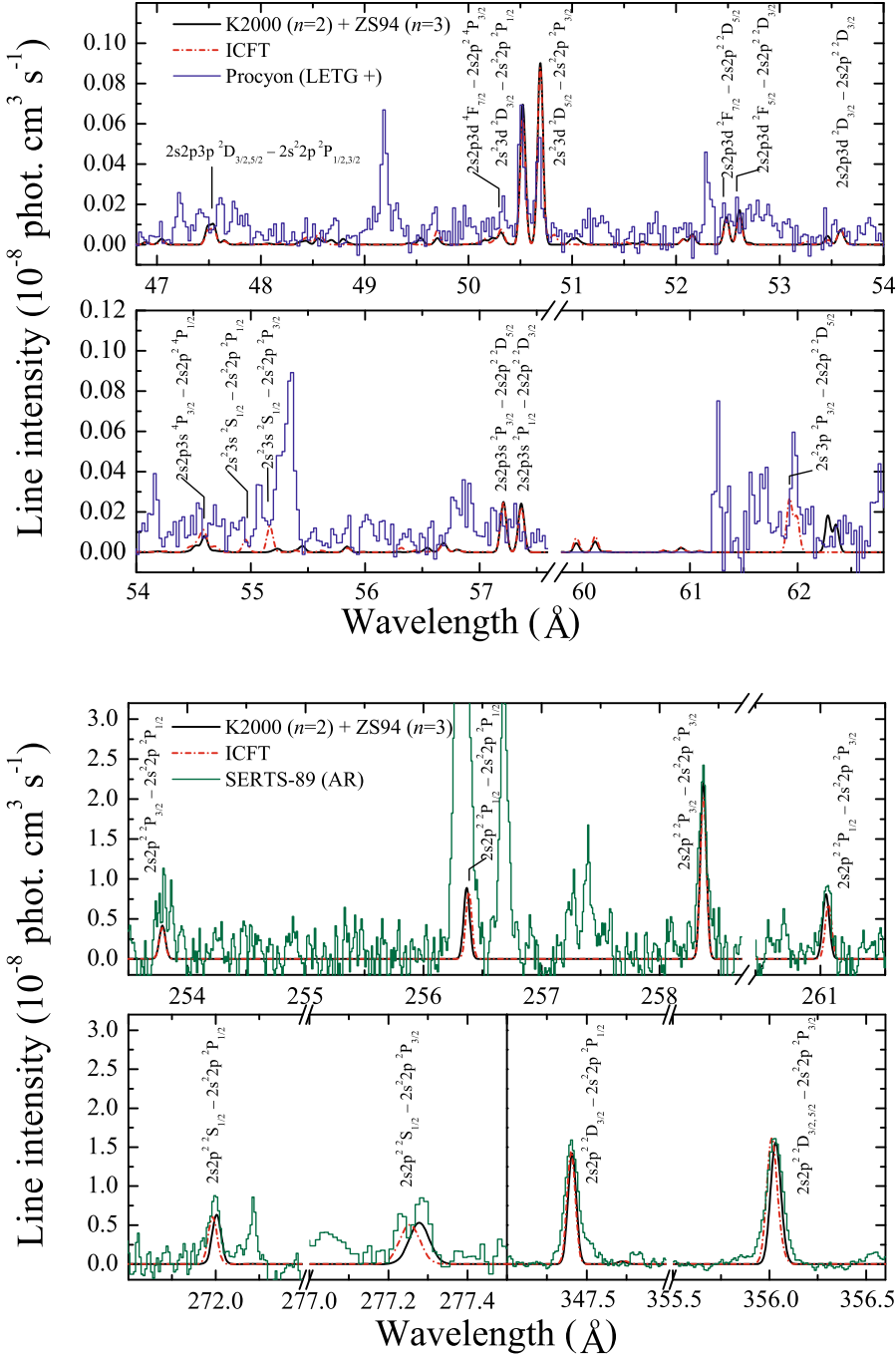
Fig. 5. Synthetic spectrum of Si X obtained by using the $n = 2$ *R*-matrix data of Keenan et al. (2000, K2000) plus the $n = 3$ DW data of Zhang & Sampson (1994, ZS94) and by using the present ICFT *R*-matrix data, and compared with observed: *top pair*, X-ray emission by *Chandra*; *bottom pair*, EUV emission by SERTS-89. The temperature and density are $T_e = 10^{6.1}$ K and $n_e = 1.6 \times 10^9$ cm^{-3}, respectively. They are typical values of the solar and Procyon coronae. A full width at half maximum (FWHM) of 60 mÅ is adopted, which is equivalent to the observed FWHM of the *Chandra* LETG observation for Procyon. (*Colour online.*)

and is higher than the present diagnosed result, as will be expanded upon in Sect. 4.

3.2. SERTS/EIS observation

For the $n = 2 \rightarrow 2$ transitions, line emissivities (ϵ) at $T_e = 10^{6.1}$ K and $n_e = 1.6 \times 10^9$ cm^{-3}, are enhanced by about 15−40% on using the present calculated data compared to that obtained on using the previous excitation data, viz. the *R*-matrix data of Keenan et al. (2000) ($n = 2$) and DW data of Zhang & Sampson (1994) ($n = 3$) (see the 5th and 8th columns in Table 4a, as well as the bottom panel in Fig. 5).

The SERTS-89 observation (see Fig. 5, lower pair) is overlapped with the present prediction by normalizing to the peak intensity of the line at 258.371 Å. For the emission at 253.81 Å, Keenan et al. (2000) attribute the large difference between theory (0.19 relative line intensity at 258.371 Å, decaying from same upper level) and the SERTS-89 observation (0.54 ± 0.21) for an active region as being due to a possible error in the observation. The Hinode/EIS observation (0.19, Brown et al. 2008) shows excellent agreement with the present prediction, which confirms Keenan et al.'s suggestion. At 256.32 Å, He II is the main contribution to the observed line flux. For other EUV lines of Si X in SERTS-89 and Hinode/EIS observations, the relative line ratios from the same upper level show good agreement between the

Table 3. a) *Chandra* LETG observation (Liang & Zhao 2008b) for Procyon along with predictions (for the line emissivity ϵ and intensity I) at $T_e = 10^{6.1}$ K and $n_e = 1.6 \times 10^9$ cm^{-3}. For completeness, an observation for a solar active region is given in the column labelled ABB85 (Acton et al. 1985). The "−" tag in the λ-columns denotes those wavelengths corrected by experimental energies.

$\lambda_{\rm obs}$ Å	Flux Procyon*	ABB85$^\triangle$	λ^a Å	ϵ^a phot. cm^3 s^{-1}	$I^a_{\rm Procyon}$	λ^b Å	ϵ^b phot. cm^3 s^{-1}	$I^b_{\rm Procyon}$	Transition Upper	Low
47.42	0.55(0.06)^c	...	−47.489	5.476(−12)^d	0.16	−47.489	4.098(−12)	0.12	2s2p3p ^{2}D$_{3/2}$ → 2s^{2}2p	^{2}P$_{1/2}$
		...	47.545	6.058(−12)	0.22	−47.545	4.831(−12)	0.14	2s2p3p ^{2}D$_{5/2}$ → 2s^{2}2p	^{2}P$_{3/2}$
50.334	0.44(0.08)	195	−50.305	1.680(−12)	0.05	−50.305	4.055(−12)	0.04	2s2p3d ^{4}D$_{5/2}$ → 2s2p^2	^{4}P$_{3/2}$
			50.316	1.259(−12)	0.04	−50.316	1.824(−12)	0.06	2s2p3d ^{2}D$_{5/2}$ → 2s2p^2	^{4}P$_{5/2}$
			−50.333	1.021(−12)	0.03	−50.333	1.477(−12)	0.04	2s2p3d ^{4}D$_{7/2}$ → 2s2p^2	^{4}P$_{5/2}$
50.524	1.38(0.09)	12	−50.524	4.403(−11)	1.26	−50.524	3.902(−11)	1.14	2s^{2}3d ^{2}D$_{3/2}$ → 2s^{2}2p	^{2}P$_{1/2}$
50.672	1.04(0.08)	74	−50.691	4.979(−11)	1.40	−50.691	4.734(−11)	1.37	2s^{2}3d ^{2}D$_{5/2}$ → 2s^{2}2p	^{2}P$_{3/2}$
			−50.703	8.778(−12)	0.25	−50.703	7.769(−12)	0.23	2s^{2}3d ^{2}D$_{3/2}$ → 2s^{2}2p	^{2}P$_{3/2}$
50.828	0.15(0.08)	...	51.047	1.224(−12)	0.04	50.829	1.812(−12)	0.06	2s2p3d ^{4}F$_{7/2}$ → 2s2p^2	^{4}P$_{5/2}$
			51.047	3.142(−13)	0.01	50.830	4.352(−13)	0.01	2s2p3d ^{4}F$_{3/2}$ → 2s2p^2	^{4}P$_{3/2}$
52.453	0.29(0.07)	15	−52.485	8.715(−12)	0.25	−52.485	7.279(−12)	0.21	2s2p3d ^{2}F$_{7/2}$ → 2s2p^2	^{2}D$_{5/2}$
52.594	0.30(0.07)	40	−52.611	1.001(−11)	0.29	−52.611	7.926(−12)	0.26	2s2p3d ^{2}F$_{5/2}$ → 2s2p^2	^{2}D$_{3/2}$
54.533	0.62(0.12)	<10	−54.521	1.564(−12)	0.04	−54.522	1.241(−12)	0.03	2s2p3s ^{4}P$_{3/2}$ → 2s2p^2	^{4}P$_{1/2}$
			−54.522	2.680(−13)	0.01	−54.522	1.302(−12)	0.04	2s2p3d ^{2}P$_{1/2}$ → 2s2p^2	^{2}S$_{1/2}$
			−54.598	4.731(−12)	0.14	−54.599	3.947(−12)	0.12	2s2p3d ^{2}P$_{3/2}$ → 2s2p^2	^{2}S$_{1/2}$
54.895	0.52(0.12)	<10	55.238	9.561(−13)	0.03	54.955	3.892(−12)	0.11	2s^{2}3s ^{2}S$_{1/2}$ → 2s^{2}2p	^{2}P$_{1/2}$
55.078	0.67(0.07)	17	55.453	1.945(−12)	0.06	55.167	8.218(−12)	0.22	2s^{2}3s ^{2}S$_{1/2}$ → 2s^{2}2p	^{2}P$_{3/2}$
57.196	0.25(0.07)	25	−57.209	1.427(−11)	0.40	−57.209	1.386(−11)	0.43	2s2p3s ^{2}P$_{3/2}$ → 2s2p^2	^{2}D$_{5/2}$
57.309	0.35(0.08)	17	−57.365	1.536(−11)	0.43	−57.365	1.459(−11)	0.40	2s2p3s ^{2}P$_{1/2}$ → 2s2p^2	^{2}D$_{3/2}$
61.971	1.11(0.14)	32	62.282	1.223(−11)	0.32	61.925	1.515(−11)	0.46	2s^{2}3p ^{2}P$_{3/2}$ → 2s2p^2	^{2}D$_{5/2,3/2}$
			62.358	8.668(−12)	0.24	61.992	1.106(−11)	0.31	2s^{2}3p ^{2}P$_{1/2}$ → 2s2p^2	^{2}D$_{3/2}$

* Units = 10^{-4} photons cm^{-2} s^{-1}; $^\triangle$ units = photons cm^{-2} s^{-1} arcsec^{-1}; ^{a} obtained using the *R*-matrix data of Keenan et al. (2000) for $n = 2$ and the DW data of Zhang & Sampson (1994) for $n = 3$; ^{b} obtained using the present ICFT *R*-matrix excitation data; ^{c} (m) denotes $\pm m$; ^{d} (n) denotes $\times 10^n$.

Table 3. b) Line intensity ratios relative to that of 50.524 Å in the soft X-ray wavelength range. The caption and footnotes are the same as in Table 3a.

$\lambda_{\rm obs}$ Å	Ratio Procyon*	ABB85$^\triangle$	λ^a Å	$I/I^a_{\rm ref}$	λ^b Å	$I/I^b_{\rm ref}$	Transition Upper	Low
47.42	0.40(0.05)^c	...	−47.489	0.12	−47.489	0.11	2s2p3p ^{2}D$_{3/2}$ → 2s^{2}2p	^{2}P$_{1/2}$
		...	47.545	0.14	−47.545	0.12	2s2p3p ^{2}D$_{5/2}$ → 2s^{2}2p	^{2}P$_{3/2}$
50.334	0.32(0.06)	16.25	−50.305	0.04	−50.305	0.10	2s2p3d ^{4}D$_{5/2}$ → 2s2p^2	^{4}P$_{3/2}$
			50.316	0.03	−50.316	0.05	2s2p3d ^{2}D$_{5/2}$ → 2s2p^2	^{4}P$_{5/2}$
			−50.333	0.02	−50.333	0.04	2s2p3d ^{4}D$_{7/2}$ → 2s2p^2	^{4}P$_{5/2}$
50.524	1.00(0.09)	1.00	−50.524	1.00	−50.524	1.00	2s^{2}3d ^{2}D$_{3/2}$ → 2s^{2}2p	^{2}P$_{1/2}$
50.672	0.75(0.08)	6.17	−50.691	1.13	−50.691	1.21	2s^{2}3d ^{2}D$_{5/2}$ → 2s^{2}2p	^{2}P$_{3/2}$
			−50.703	0.20	−50.703	0.20	2s^{2}3d ^{2}D$_{3/2}$ → 2s^{2}2p	^{2}P$_{3/2}$
50.828	0.11(0.06)	...	51.047	0.03	50.829	0.05	2s2p3d ^{4}F$_{7/2}$ → 2s2p^2	^{4}P$_{5/2}$
			51.047	0.01	50.830	0.01	2s2p3d ^{4}F$_{3/2}$ → 2s2p^2	^{4}P$_{3/2}$
52.453	0.21(0.05)	1.25	−52.485	0.20	−52.485	0.19	2s2p3d ^{2}F$_{7/2}$ → 2s2p^2	^{2}D$_{5/2}$
52.594	0.22(0.05)	3.33	−52.611	0.23	−52.611	0.20	2s2p3d ^{2}F$_{5/2}$ → 2s2p^2	^{2}D$_{3/2}$
54.533	0.45(0.09)	<1.00	−54.521	0.04	−54.522	0.03	2s2p3s ^{4}P$_{3/2}$ → 2s2p^2	^{4}P$_{1/2}$
			−54.522	0.01	−54.522	0.03	2s2p3d ^{2}P$_{1/2}$ → 2s2p^2	^{2}S$_{1/2}$
			−54.598	0.11	−54.599	0.10	2s2p3d ^{2}P$_{3/2}$ → 2s2p^2	^{2}S$_{1/2}$
54.895	0.38(0.09)	<1.00	55.238	0.02	54.955	0.10	2s^{2}3s ^{2}S$_{1/2}$ → 2s^{2}2p	^{2}P$_{1/2}$
55.078	0.49(0.06)	1.42	55.453	0.04	55.167	0.21	2s^{2}3s ^{2}S$_{1/2}$ → 2s^{2}2p	^{2}P$_{3/2}$
57.196	0.18(0.05)	2.08	−57.209	0.32	−57.209	0.36	2s2p3s ^{2}P$_{3/2}$ → 2s2p^2	^{2}D$_{5/2}$
57.309	0.25(0.06)	1.42	−57.365	0.35	−57.365	0.37	2s2p3s ^{2}P$_{1/2}$ → 2s2p^2	^{2}D$_{3/2}$
61.971	0.80(0.11)	2.67	62.282	0.28	61.925	0.39	2s^{2}3p ^{2}P$_{3/2}$ → 2s2p^2	^{2}D$_{5/2,3/2}$
			62.358	0.20	61.992	0.28	2s^{2}3p ^{2}P$_{1/2}$ → 2s2p^2	^{2}D$_{3/2}$

observations and the theoretical prediction, see Table 4b. However, line intensities at 261.05 Å, 271.99 Å and 277.27 Å, relative to that at 258.37 Å, are lower than the observation's by $\approx 8-21\%$. This is due to the slightly higher electron density used (1.6×10^6 cm^{-3}, taken from the diagnostic value of Keenan et al. 2000), than we predict next.

3.3. SUMER observation

The wavelengths of transitions amongst the 4 lowest-lying levels fall in the $600-650$ Å range. The enhancement of line emissivity (ϵ) is about $40-60\%$ on using the present ICFT *R*-matrix data compared to that obtained using previous excitation data, viz.

Table 4. a) SERTS/EIS observation (Keenan et al. 2000; Brown et al. 2008) for a solar active region along with predictions (for the line emissivity ϵ and intensity I, based upon the observed line flux at 258.37 Å) at $T_e = 10^{6.1}$ K and $n_e = 1.6 \times 10^9$ cm^{-3}. The "−" tag in the λ-columns denotes those wavelengths corrected by experimental energies.

λ_{obs} Å	Flux SERTS[†]	Flux EIS[†]	λ^a Å	ϵ^a phot. cm^3 s^{-1}	I^a_{SERTS}	λ^b Å	ϵ^b phot. cm^3 s^{-1}	I^b_{SERTS}	Transition Upper	Transition Low
253.81	3.28(1.02)^c	86.8	−253.788	2.273(−10)^d	1.15	−253.787	2.762(−10)	1.18	2s2p^2 ^{2}P$_{3/2}$	→ 2s^{2}2p ^{2}P$_{1/2}$
256.32	25.26(5.06)	462.5	−256.366	4.858(−10)	2.46	−256.384	6.036(−10)	2.57	2s2p^2 ^{2}P$_{1/2}$	→ 2s^{2}2p ^{2}P$_{1/2}$
258.37	6.08(1.35)	452.3	−258.371	1.203(−09)	6.08	−258.371	1.427(−09)	6.08	2s2p^2 ^{2}P$_{3/2}$	→ 2s^{2}2p ^{2}P$_{3/2}$
261.05	2.28(0.57)	17.1	−261.044	4.424(−10)	2.24	−261.063	4.909(−10)	2.09	2s2p^2 ^{2}P$_{1/2}$	→ 2s^{2}2p ^{2}P$_{3/2}$
271.99	2.22(0.56)	152.3	−272.006	3.466(−10)	1.75	−271.983	4.378(−10)	1.87	2s2p^2 ^{2}S$_{1/2}$	→ 2s^{2}2p ^{2}P$_{1/2}$
277.27	1.97(0.54)	116.5	−277.278	2.891(−10)	1.46	−277.254	3.665(−10)	1.56	2s2p^2 ^{2}S$_{1/2}$	→ 2s^{2}2p ^{2}P$_{3/2}$
347.41	4.55(1.27)	...	−347.409	7.764(−10)	3.92	−347.403	1.011(−09)	4.31	2s2p^2 ^{2}D$_{3/2}$	→ 2s^{2}2p ^{2}P$_{1/2}$
356.03	4.84(0.56)	...	−356.030	7.786(−10)	3.94	−356.011	1.090(−09)	4.64	2s2p^2 ^{2}D$_{5/2}$	→ 2s^{2}2p ^{2}P$_{3/2}$
			−356.055	1.137(−10)	0.57	−356.050	1.483(−10)	0.63	2s2p^2 ^{2}D$_{3/2}$	→ 2s^{2}2p ^{2}P$_{3/2}$

† Units = 10^{12} photons cm^{-2} s^{-1} sr^{-1}; ^{a,b,c,d} the same definition as in Table 3a.

Table 4. b) Line intensity ratios relative to that of 258.37 Å for the SERTS/EIS observation. The caption and footnotes are the same as in Table 4a.

λ_{obs} Å	Ratio SERTS[†]	Ratio EIS[†]	λ^a Å	I/I^a_{ref}	λ^b Å	I/I^b_{ref}	Transition Upper	Transition Low
253.81	0.54(0.21)	0.19	−253.788	0.19	−253.787	0.19	2s2p^2 ^{2}P$_{3/2}$	→ 2s^{2}2p ^{2}P$_{1/2}$
256.32	4.15(1.24)	1.02	−256.366	0.40	−256.384	0.42	2s2p^2 ^{2}P$_{1/2}$	→ 2s^{2}2p ^{2}P$_{1/2}$
258.37	1.00(0.31)	1.00	−258.371	1.00	−258.371	1.00	2s2p^2 ^{2}P$_{3/2}$	→ 2s^{2}2p ^{2}P$_{3/2}$
261.05	0.38(0.13)	0.04	−261.044	0.37	−261.063	0.34	2s2p^2 ^{2}P$_{1/2}$	→ 2s^{2}2p ^{2}P$_{3/2}$
271.99	0.37(0.12)	0.34	−272.006	0.29	−271.983	0.31	2s2p^2 ^{2}S$_{1/2}$	→ 2s^{2}2p ^{2}P$_{1/2}$
277.27	0.32(0.11)	0.26	−277.278	0.24	−277.254	0.26	2s2p^2 ^{2}S$_{1/2}$	→ 2s^{2}2p ^{2}P$_{3/2}$
347.41	0.75(0.27)	...	−347.409	0.65	−347.403	0.71	2s2p^2 ^{2}D$_{3/2}$	→ 2s^{2}2p ^{2}P$_{1/2}$
356.03	0.80(0.20)	...	−356.030	0.65	−356.011	0.76	2s2p^2 ^{2}D$_{5/2}$	→ 2s^{2}2p ^{2}P$_{3/2}$
			−356.055	0.09	−356.050	0.10	2s2p^2 ^{2}D$_{3/2}$	→ 2s^{2}2p ^{2}P$_{3/2}$

Table 5. a) SUMER observation for the quiet sun (Curdt et al. 2004) along with predictions (for the line emissivity ϵ and intensity I, based upon the observed line flux at 638.92 Å) at $T_e = 10^{6.1}$ K and $n_e = 1.6 \times 10^9$ cm^{-3}. The "−" tag in the λ-columns denotes those wavelengths corrected by experimental energies.

λ_{obs} Å	Flux[‡]	λ^a Å	ϵ^a phot. cm^3 s^{-1}	I^a	λ^b Å	ϵ^b phot. cm^3 s^{-1}	I^b	Transition Upper	Transition Low
611.61	0.77	−611.712	7.399(−12)^d	0.72	−611.712	1.083(−11)	0.72	2s2p^2 ^{4}P$_{3/2}$	→ 2s^{2}2p ^{2}P$_{1/2}$
621.11		−621.115	2.303(−11)	2.23	−621.080	3.291(−11)	2.18	2s2p^2 ^{4}P$_{1/2}$	→ 2s^{2}2p ^{2}P$_{1/2}$
624.71	8.40	−624.779	9.531(−11)	9.24	−624.730	1.498(−10)	9.92	2s2p^2 ^{4}P$_{5/2}$	→ 2s^{2}2p ^{2}P$_{3/2}$
638.92	6.60	−639.036	6.807(−11)	6.60	−639.036	9.965(−11)	6.60	2s2p^2 ^{4}P$_{3/2}$	→ 2s^{2}2p ^{2}P$_{3/2}$
649.21	1.90	−649.305	1.701(−11)	1.65	−649.269	2.573(−11)	1.70	2s2p^2 ^{4}P$_{1/2}$	→ 2s^{2}2p ^{2}P$_{3/2}$

‡ Units = photons cm^{-2} s^{-1} arcsec^{-1}; ^{a,b,d} the same definition as in Table 3a.

Table 5. b) Line intensity ratios relative to that of 638.92 Å in the SUMER observation. The caption and footnotes are the same as in Table 5a.

λ_{obs} Å	Ratio	λ^a Å	I/I^a_{ref}	λ^b Å	I/I^b_{ref}	Transition Upper	Transition Low
611.61	0.12	−611.712	0.11	−611.712	0.11	2s2p^2 ^{4}P$_{3/2}$	→ 2s^{2}2p ^{2}P$_{1/2}$
621.11		−621.115	0.34	−621.080	0.33	2s2p^2 ^{4}P$_{1/2}$	→ 2s^{2}2p ^{2}P$_{1/2}$
624.71	1.27	−624.779	1.40	−624.730	1.50	2s2p^2 ^{4}P$_{5/2}$	→ 2s^{2}2p ^{2}P$_{3/2}$
638.92	1.00	−639.036	1.00	−639.036	1.00	2s2p^2 ^{4}P$_{3/2}$	→ 2s^{2}2p ^{2}P$_{3/2}$
649.21	0.29	−649.305	0.25	−649.269	0.26	2s2p^2 ^{4}P$_{1/2}$	→ 2s^{2}2p ^{2}P$_{3/2}$

the *R*-matrix data of Keenan et al. (2000) ($n = 2$) and DW data of Zhang & Sampson (1994) ($n = 3$), see Table 5a. However, the relative line emissivity (ratio) shows excellent agreement between the two different models (see Table 5b).

Based upon the observed flux of the well known emission at 638.92 Å, we made a comparison with a SUMER observation

for the quiet sun (Curdt et al. 2004). Table 5b shows that there is a good agreement between the present prediction and the SUMER observation reported by Curdt et al. (2004). Moreover, an additional feature for Si X is predicted at 621.11 Å, with intensity 0.33, which confirms the suggestion by Curdt et al. (2004) that the emission at 1242 Å may be from the
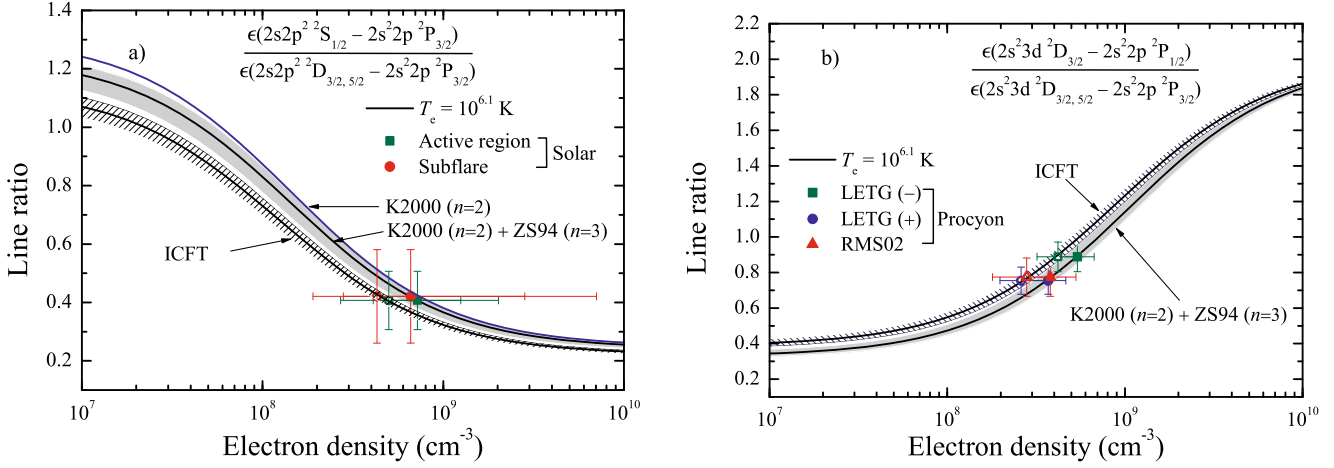
Fig. 6. Line intensity ratios as a function of electron density (cm^{-3}). **a)**: R_8, symbols with errors are solar observations for an active region and a sub-flare, from Keenan et al. (2000), and the estimated electron densities from the depicted line ratios. **b)**: R_{X-ray}, symbols with errors corresponding to observations of the Procyon coronae, from Liang & Zhao (2008b), and the estimated electron densities from the depicted line ratios. RMS02 denotes the work of Raassen et al. (2002). In both, the hatched region uses from the present ICFT *R*-matrix data and the grey region uses the $n = 2$ *R*-matrix data of Keenan et al. (2000, K2000) plus the $n = 3$ DW data of Zhang & Sampson (1994, ZS94). The regions indicate the ratio between the temperatures $T_e = 10^{6.0-6.2}$ K, while the solid lines correspond to a temperature of $T_e = 10^{6.1}$ K, at which Si^{9+} has its peak abundance in collisional equilibrium. (*Colour online.*)

Fe XII feature at 1242.004 Å ($2s^22p^3\ ^2P_{3/2} \rightarrow 2s^23p^3\ ^4S_{3/2}$) and a second-order spectral line of Si X at 621.11 Å.

4. Diagnostic of the electron density

Keenan et al. (2000) explored n_e-sensitive line ratios of EUV transitions lines of Si X. For example,

$$R_3 = \frac{\epsilon(2s2p^2\ ^2S_{1/2} - 2s^22p\ ^2P_{1/2})}{\epsilon(2s2p^2\ ^2D_{3/2,5/2} - 2s^22p\ ^2P_{3/2})},$$

$$R_5 = \frac{\epsilon(2s2p^2\ ^2D_{3/2} - 2s^22p\ ^2P_{1/2})}{\epsilon(2s2p^2\ ^2D_{3/2,5/2} - 2s^22p\ ^2P_{3/2})},$$

$$R_7 = \frac{\epsilon(2s2p^2\ ^2P_{1/2} - 2s^22p\ ^2P_{3/2})}{\epsilon(2s2p^2\ ^2D_{3/2,5/2} - 2s^22p\ ^2P_{3/2})} \text{ and}$$

$$R_8 = \frac{\epsilon(2s2p^2\ ^2S_{1/2} - 2s^22p\ ^2P_{3/2})}{\epsilon(2s2p^2\ ^2D_{3/2,5/2} - 2s^22p\ ^2P_{3/2})}.$$

Liang & Zhao (2008b) reported the line ratio (R_{X-ray}) of $\epsilon(50.524$ Å$)$ versus $\epsilon(50.691$ Å $+50.703$ Å$)$ as a powerful n_e-diagnostic. Here, we calculate these line ratios as a function of the electron density, and explore the effect of our resonance-enhanced excitation data on line ratios and the resultant electron densities for the Procyon and solar coronae.

By comparing the observed line ratio with the theoretical prediction, we derived the electron density in the line-emitting region of the astrophysical plasma[15]. As seen in Fig. 6, for R_8, the estimated n_e from the present data (including soft X-ray and EUV emissions) is lower than that obtained from the data of Keenan et al. (2000) ($n = 2$) plus Zhang & Sampson (1994) ($n = 3$), although they agree to within 1σ. This downward shift of the
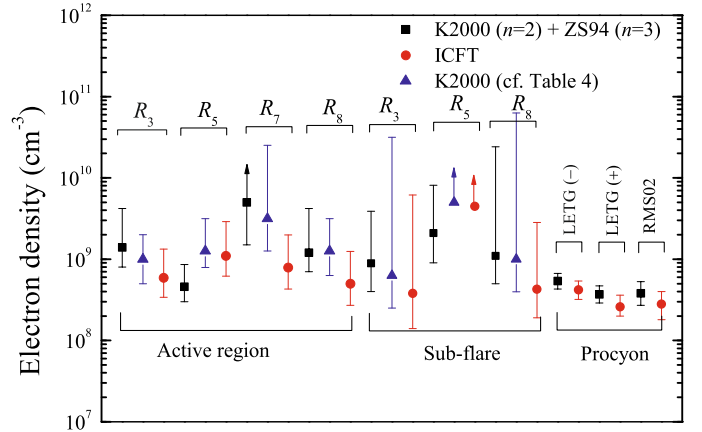
---
[15] We note that Keenan et al. (2000) determined (asymmetric) error bars on the electron density by evaluating the density at the error bars of the measured line ratio – we repeat this simplistic procedure to facilitate comparison with Keenan et al. (2000).

Fig. 7. Diagnosed electron densities from the line ratios R_3, R_5, R_7 and R_8 for a solar active region and a sub-flare, as well as from R_{X-ray} for the Procyon corona, obtained by using EUV and soft X-ray emissions of Si X, respectively. The "square" symbols denote the estimate obtained from the $n = 2$ *R*-matrix data of Keenan et al. (2000, K2000) plus the $n = 3$ DW data of Zhang & Sampson (1994, ZS94); the "circle" symbols correspond to results obtained using the present ICFT *R*-matrix data; the "triangle" symbols show the results of Keenan et al. (2000, cf. Table 4). LETG (−) and LETG (+) correspond to the *Chandra*/LETG negative and positive observations, respectively. RMS02 refers to the work of Raassen et al. (2002). (*Colour online.*)

predicted n_e is due to the resonance-enhanced $n = 2 \rightarrow 3$ collisional excitations.

Since only $n = 2$ levels have been included by Keenan et al., we also tested the effect of radiative cascades from $n = 3$ levels following excitations to them, as done in CHIANTI v5.2. As seen in Fig. 6a, the line ratio is slightly shifted upwards (5% at at $n_e = 2.0 \times 10^8$ cm^{-3}) when only $n = 2$ levels are taken into account. This may be the reason that the estimation of Keenan et al. (2000) is higher the present one.

From other line ratios R_3, R_5 and R_7, we derived the electron density and obtained a mean value of $7.5^{+1.3}_{-2.7} \times 10^8$ cm^{-3} and $1.8^{+1.4}_{-2.4} \times 10^9$ cm^{-3} for a solar active region and a sub-flare,

respectively, which is lower than the upper limits $(2.9 \times 10^9$ cm^{-3} and 6.3×10^{10} cm$^{-3})$ of Keenan et al. (2000). For Procyon, the present result $(3.2^{+2.0}_{-1.5} \times 10^8$ cm$^{-3})$ is also slightly lower than that $(4.3^{+2.2}_{-1.7} \times 10^8$ cm$^{-3})$ we obtained from using the atomic data of Keenan et al. (2000) $(n = 2)$ plus Zhang & Sampson (1994) $(n = 3)$.

5. Summary

Electron-impact excitation data for B-like Si has been calculated, using the ICFT *R*-matrix method, between the 125 fine-structure levels (58 LS terms) belonging to the configurations $2s^x 2p^y$ $(x + y = 3)$ and $2s^\alpha 2p^\beta 3l$ $(\alpha + \beta = 2$, $l = $ s, p and d). For some $n = 2 \rightarrow 2$ excitation rates with $\Upsilon < 0.1$, the present results are higher than those of Keenan et al. (2000). Moreover, the enhancement can be more than a factor of 2. This is most likely due to resonances attached to $n = 3$ which were not described by Keenan et al. Furthermore, at high temperatures, we observed incongruous behaviour in their effective collision strengths for many dipole transitions. For the $n = 2 \rightarrow 3$ excitation rates, the present results are higher than previously available (Zhang & Sampson 1994 and Liang et al. 2007) non-resonant DW data, and can be so by more than an order of magnitude for many transitions at low temperatures $(\lesssim 5 \times 10^5$ K). Here, the difference peaks in the range $1 \times 10^4 \lesssim T_e(\text{K}) \lesssim 1 \times 10^5$, and so is of likely importance for photoionized plasmas.

Using our new atomic data, we derived line emissivities at equilibrium. For some EUV lines, their emissivities are enhanced by 20−60%. This enhancement will result in the decreasing of the emission measure for an astrophysical plasma. Additionally, comparisons with an LETG observation for Procyon, a SERTS observation for a solar active region and SUMER observation have been made. Correspondingly, a brief comparison was made with the soft X-ray observation for a solar flare by Acton et al. (1985), and with an Hinode/EIS observation. We found that the 3s−2p transition lines at 55.167 Å are enhanced by a factor of 5 in the present model, which satisfactorily explains the discrepancy between the LETG observation for Procyon and the prediction in work of Liang et al. (2008b). For the emissions at 47.420 Å and 61.971 Å, the present model estimates the contributions to the observed line fluxes from Si X to be 83% and 84%, respectively. Results of the present structure calculation lead to the wavelength of the $2s^2 3p\ ^2P_{3/2} - 2s2p^2\ ^2D_{5/2}$ transition showing a better agreement with the observed value of 61.971 Å.

The calculated line ratios shift upward/downward using the present calculated atomic data when compared with that using previous data including *R*-matrix data for $n = 2$ levels (Keenan et al. 2000) and DW data for $n = 3$ levels (Zhang & Sampson 1994). Estimated electron densities from these line ratios shift downward due to the resonant-enhancement of the $n = 2 \rightarrow 3$ excitation data used in the present model. For example, in case of Procyon, the density decreases from $4.3^{+2.2}_{-1.7} \times 10^8$ cm^{-3} to $3.2^{+2.0}_{-1.5} \times 10^8$ cm^{-3}.

In conclusion, we have demonstrated the significant improvement of the excitation data of Si^{9+}, and its effect on the diagnostic modelling of astrophysical spectra. The extensive excitation data determined by way of the ICFT *R*-matrix method will significantly improve the accuracy of astrophysical spectral analysis.

References

Acton, L. W., Bruner, M. E., Brown, W. A., et al. 1985, ApJ, 291, 865
Audard, M., Behar, E., Güdel, M., et al. 2001, A&A, 365, L329
Badnell, N. R. 1997, J. Phys. B: At. Mol. Opt. Phys., 30, 1
Badnell, N. R., & Griffin, D. C. 2001, J. Phys. B: At. Mol. Opt. Phys., 34, 681
Bar-Shalom, A., Klapisch, M., & Oreg, J. 1988, Phys. Rev. A, 38, 1773
Beiersdorfer, P., Behar, E., Boyce, K. R., et al. 2002, ApJ, 576, L169
Beiersdorfer, P., Bitter, M., von Goeler, S., et al. 2004, ApJ, 610, 616
Brown, C. M., Feldman, U., Seely, J. F., et al. 2008, ApJS, 176, 511
Bryans, P., Badnell, N. R., Gorczyca, T. W., et al. 2006, ApJS, 167, 343
Burgess, A. 1974, J. Phys. B: At. Mol. Opt. Phys., 7, L364
Burgess, A., & Tully, J. A. 1992, A&A, 254, 436
Cavalcanti, G. H., Luna, F. R. T., & Trigueiros, A. G. 2000, J. Quant. Spectrosc. Radiat. Transfer, 64, 5
Curdt, W., Landi, E., & Feldman, U. 2002, A&A, 427, 1045
Del Zanna, G. 2006, A&A, 459, 307
Del Zanna, G., & Mason, H. E. 2003, A&A, 406, 1089
Desai, P., Brickhouse, N. S., Drake, J. J., et al. 2005, ApJ, 625, L59
Doron, R., & Behar, E. 2002, ApJ, 574, 518
Foster, V. J., Keenan, F. P., & Reid, R. H. G. 1997, At. Data and Nucl. Data Tables, 67, 99
Griffin, D. C., Badnell, N. R., & Pindzola, M. S. 1998, J. Phys. B: At. Mol. Opt. Phys., 31, 3713
Gu, M. F. 2003, ApJ, 582, 1241
Gu, M. F., Beiersdorfer, P., Brown, G. V., et al. 2004, ApJ, 607, L143
Kallman, T., & Bautista, M. 2001, ApJS, 133, 221
Keenan, F. P., O'Shea, E., Thomas, R. J., et al. 2000, MNRAS, 315, 450
Keenan, F. P., Katsiyannis, A. C., Reid, R. H. G., et al. 2003, MNRAS, 346, 58
Flower, D. R., & Nussbaumer, H. 1975, A&A, 45, 349
Landi, E., Del Zanna, G., Young, P. R., et al. 2006, ApJS, 162, 261
Lepson, J. K., Beiersdorfer, P., Behar, E., et al. 2003, ApJ, 590, 604
Lepson, J. K., Beiersdorfer, P., Behar, E., et al. 2005, ApJ, 625, 1045
Liang, G. Y., & Zhao, G. 2008a, AJ, 135, 2291
Liang, G. Y., & Zhao, G. 2008b, MNRAS, 384, 489
Liang, G. Y., Zhao, G., & Zeng, J. L. 2007, At. Data and Nucl. Data Tables, 93, 375
Mazzotta, P., Mazzitelli, G., Colafrancesco, S., et al. 1998, A&AS, 133, 403
Mewe, R., Raassen, A. J. J., Drake, J. J., et al. 2001, A&A, 367, 282
Phillips, K. J. H., Bhatia, A. K., Mason, H. E., et al. 1996, ApJ, 466, 549
Raassen, A. J. J., Mewe, R., Audard, M., et al. 2002, A&A, 389, 228
Savin, D. W., Behar, E., Kahn, S. M., et al. 2002, ApJS, 138, 337
Saba, J. L. R., Schmelz, J. T., Bhatia, A. K., & Strong, K. T. 1999, ApJ, 510, 1064
Schmelz, J. T., Saba, J. L. R., Chauvin, J. C., & Strong, K. T. 1997, ApJ, 477, 509
Schrijver, C. J., van den Oord, G. H. J., & Mewe, R. 1994, A&A, 289, L23
Smith, R. K., Brickhouse, N. S., Liedahl, D. A., et al. 2001, ApJ, 556, L91
Summers, H. P. 2004, The ADAS User Manual – version 2.6 (http://www.adas.ac.uk)
Thomas, R. J., & Neupert, W. M. 1994, ApJS, 91, 461
Wargelin, B. J., Beiersdorfer, P., Liedahl, D. A., et al. 1998, ApJ, 496, 1031
Witthoeft, M. C., & Badnell, N. R. 2008, A&A, 481, 543
Witthoeft, M. C., Badnell, N. R., Del Zanna, G., et al. 2006, A&A, 446, 361
Zhang, H. L., & Sampson, D. H. 1994, At. Data and Nucl. Data Tables, 58, 255
Zhang, H. L., Graziani, M., & Pradhan, A. K. 1994, A&A, 283, 319